

ARTICLE

<https://doi.org/10.1038/s42005-019-0278-6>

OPEN

# Mechanisms of blueshifts in organic polariton condensates

Timur Yagafarov<sup>1,9</sup>, Denis Sannikov <sup>1,2,9</sup>, Anton Zasedatelev <sup>1,9\*</sup>, Kyriacos Georgiou<sup>3</sup>, Anton Baranikov<sup>1</sup>, Oleksandr Kyriienko <sup>4,5</sup>, Ivan Shelykh<sup>5,6</sup>, Lizhi Gai<sup>7</sup>, Zhen Shen <sup>7</sup>, David Lidzey <sup>3</sup> & Pavlos Lagoudakis<sup>1,8</sup>

Bose-Einstein condensates of exciton-polaritons in inorganic semiconductor microcavities are known to possess strong interparticle interactions attributed to their excitonic component. The interactions play a crucial role in the nonlinear dynamics of such systems and can be witnessed as the energy blueshifts of polariton states. However, the localised nature of Frenkel excitons in strongly coupled organic microcavities precludes interparticle Coulomb exchange-interactions that change mechanisms of the nonlinearity and blueshifts accordingly. In this report, we unravel the origins of blueshifts in organic polariton condensates. We examine the possible contributions: intracavity optical Kerr-effect, gain-induced frequency-pulling, polariton interactions and effects related to saturation of optical transitions for weakly- and strongly-coupled molecules. We conclude that blueshifts in organic polariton condensates arise from the interplay of the saturation effects and intermolecular energy migration. Our model predicts the commonly observed step-like increase of both the emission energy and degree of linear polarization at the polariton condensation threshold.

<sup>1</sup>Center of Photonics and Quantum Materials, Skolkovo Institute of Science and Technology, Moscow, Russian Federation 121205. <sup>2</sup>Lebedev Physical Institute of the Russian Academy of Sciences, Moscow, Russian Federation 119333. <sup>3</sup>Department of Physics and Astronomy, University of Sheffield, Sheffield S3 7RH, UK. <sup>4</sup>Department of Physics and Astronomy, University of Exeter, Stocker Road, Exeter EX4 4QL, UK. <sup>5</sup>ITMO University, Saint Petersburg, Russian Federation 197101. <sup>6</sup>Science Institute, University of Iceland, Dunhagi-3, IS-107 Reykjavik, Iceland. <sup>7</sup>State Key Laboratory of Coordination and Chemistry, School of Chemistry and Chemical Engineering, Nanjing University, 210046 Nanjing, China. <sup>8</sup>Department of Physics and Astronomy, University of Southampton, Southampton SO17 1BJ, UK. <sup>9</sup>These authors contributed equally: Timur Yagafarov, Denis Sannikov, Anton Zasedatelev. \*email: [a.zasedatelev@skoltech.ru](mailto:a.zasedatelev@skoltech.ru)

Electronic excitations in organic semiconductors can be described in terms of Frenkel excitons in which strongly bound electron–hole pairs are localized on a single molecule. Frenkel excitons typically have a binding energy of the order of 0.5–1 eV that allows them to survive at ambient temperatures. Following the first observation of strong coupling in organic microcavities<sup>1</sup>, the rapid development of polariton photonics has culminated in the observation of polariton condensates at room temperature. Emission wavelengths spanning the visible spectrum have been demonstrated through the selection of appropriate molecular materials<sup>2–8</sup>. Furthermore, polariton condensation in organic microcavities has led to the demonstration of polariton transistors operating at ambient conditions having a record-high optical gain ( $\sim 10$  dB  $\mu\text{m}^{-1}$ )<sup>9</sup>. The coherent nature of organic polariton condensates also results in superfluid propagation<sup>10</sup>, suggesting further applications in polariton circuits.

Despite the rapid progress of organic photonics and their potential for applications, the mechanisms underlying polariton nonlinearities remain poorly understood. In organic semiconductors, the localization of Frenkel excitons on a single molecule dramatically weakens Coulomb exchange interactions and interparticle scattering. The blueshift of a polariton mode is considered a key manifestation of polariton interactions in inorganic microcavities<sup>11,12</sup>. However, in organic polariton systems, the origin of a step-like energy shift observed at condensation thresholds remains unclear, despite its omnipresence across a diverse range of organic materials<sup>3–9</sup>.

In this article, we explore the origin of blueshifts in organic polariton condensates. We examine the relative contribution of a number of processes, including intracavity optical Kerr effect, gain-induced frequency pulling, polariton–exciton and polariton–polariton scattering, as well as the quenching of the Rabi splitting and renormalization of the cavity mode energy both induced by the saturation of molecular optical transitions due to states filling at higher excitation densities (Pauli blocking). Through a quantitative analysis, we conclude that the blueshifts in organic polariton condensates and the step-like energy increase, observed at threshold<sup>3–9</sup>, result from an interplay between stimulated relaxation to the polariton ground state and intermolecular energy transfer. The latter process results in a depolarization of the emission with respect to the polarization of the excitation beam. Our interpretation is qualitatively and quantitatively corroborated by a concomitant step-like increase of the degree of linear polarization of the emission at condensation threshold<sup>3–5,8</sup>.

## Results

**Strong coupling.** The organic microcavities studied here, consisted of a  $\sim \lambda/2$  spin-cast thin film of BODIPY-G1 dye uniformly dispersed in a polystyrene matrix (see Supplementary Note 1) that was positioned between two distributed Bragg reflectors (DBRs) consisting of 8 and 10 pairs of  $\text{SiO}_2/\text{Nb}_2\text{O}_5$  placed on the top and bottom of the structure, respectively. For more information about sample fabrication, see Methods. We have found that the spin-casting process used to deposit the organic film results in a gradual increase of film thickness towards the edges of the substrate (bottom mirror). We use this non-uniformity to access a broad range of exciton–photon detuning ( $\delta$ ).

We measure angle-resolved reflectivity of a typical microcavity, as shown in Fig. 1a. Here both upper and lower polariton branches can be observed as local minima in the broad DBR reflectivity stop-band that are split around the BODIPY-G1 peak absorption wavelength at 507 nm. For further experimental details, see Methods. We plot the energy of these modes as a function of angle, creating a dispersion plot as shown in Fig. 1b (red squares). These data are superimposed over a false-color plot

of polariton photoluminescence intensity obtained under non-resonant excitation at 400 nm in the linear excitation regime. We fit the upper and lower polariton branches in Fig. 1b using a two coupled-oscillator model<sup>13,14</sup>, and obtain a vacuum Rabi splitting ( $\hbar\Omega_0$ ) of  $\sim 116$  meV and an exciton–photon detuning of  $-160$  meV (further details are given in Supplementary Note 2).

**Blueshifts in polariton condensates.** Recent studies have shown that a number of the BODIPY family of molecular dyes undergo polariton condensation/lasing following non-resonant optical excitation<sup>6,7</sup>. To demonstrate condensation using BODIPY-G1, we record the dispersion of polariton photoluminescence emission as a function of excitation density using single excitation pulses in a transmission configuration (see Methods). The excitation laser used provides 2 ps pulses at 400 nm having a horizontal polarization. Figure 2a shows the time-integrated polariton photoluminescence distributed across the lower polariton branch below condensation threshold. Figure 2b shows microcavity emission above-threshold, where it can be seen that polariton photoluminescence collapses to the bottom of the lower polariton branch. In Fig. 2c we plot the photoluminescence intensity and the full-width at half-maximum of the emission linewidth (right axis, in red) integrated over  $\pm 1^\circ$  ( $\pm 0.2 \mu\text{m}^{-1}$ ) around normal incidence versus excitation density. The corresponding energy shift and the degree of linear polarization of the emission spectrum are also shown in Fig. 2d, e, respectively. At an excitation density of  $\sim 6 \text{ mJ cm}^{-2}$  ( $120 \mu\text{J cm}^{-2}$  of absorbed pump fluence), we observe a rapid increase of the photoluminescence intensity, a concomitant linewidth narrowing from 1.6 to 0.25 nm and a step-like increase of the degree of linear polarization and a step-like blueshift of the emission spectrum. Such blueshifts of the polariton emission wavelength occurring around a lasing threshold are commonly considered a hallmark of polariton condensation. In inorganic semiconductor microcavities, such energy shifts originate from the repulsive interparticle Coulomb exchange interactions between Wannier–Mott excitons<sup>15</sup>. However, such interactions are in principle precluded in polaritons created using molecular semiconductors as a result of the highly localized nature of Frenkel excitons<sup>16,17</sup>.

To explore the mechanism behind such blueshifts, we examine the contribution of various nonlinear optical phenomena, omnipresent both in the strong- and weak-coupling regimes, namely the intracavity optical Kerr effect, the gain-induced frequency pulling, and interparticle interactions.

**Optical Kerr effect.** A step-like increase in the intensity of the electric field inside the cavity at condensation threshold (determined at the lower polariton mode wavelength) could potentially shift the resonance through a change in the nonlinear refractive index of the intracavity material by means of the conventional Kerr effect. To examine the contribution of the  $E$ -field induced difference in the refractive index, we measure the optical nonlinearities of the bare intracavity medium using both a closed- and open-aperture Z-scan technique<sup>18</sup> (for details, see Supplementary Note 3 and Methods). Figure 3a shows an open-aperture Z-scan transmission recorded at two pulse energies, probing the imaginary part of the nonlinear susceptibility. We find that at the lower incident pulse energy of 9.5 nJ, we do not observe any nonlinear change of the absorption. We note that at the foci, the 9.5 nJ excitation pulse induces an electric-field intensity of  $17 \text{ GW cm}^{-2}$ ; a value that is approximately an order of magnitude higher than the electric-field intensity at the anti-node within the microcavity at  $1.4 P_{\text{th}}$  ( $\sim 2 \text{ GW cm}^{-2}$ ) (calculation is shown in Supplementary Note 4). At the considerable higher intensity of

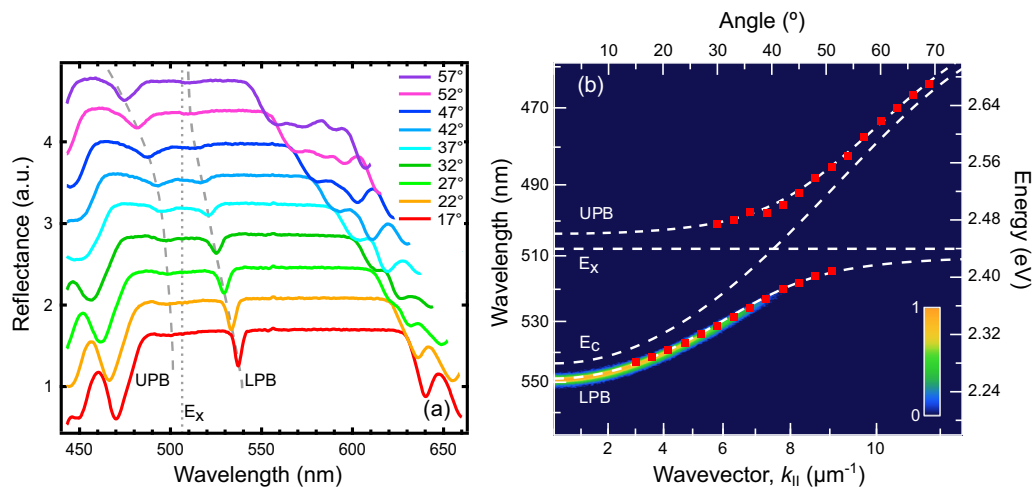


**Fig. 1 Strong light-matter interaction in the dye-filled microcavity.** **a** Angle-dependent reflectivity spectra of the microcavity recorded at different angles exhibit clear anti-crossing at the exciton resonance energy  $E_x$  (gray dotted line) and indicate the formation of lower (LPB, gray dashed line) and upper (UPB, gray dashed line) exciton-polariton branches. Polariton dispersion relation in **b** is plotted by combing the data of photoluminescence imaging acquired in a Fourier space (rainbow color density plot in a log scale) with the polariton states extracted from angle-dependent reflectivity measurements (red squares). Error bars are within the marker size and correspond to standard deviations of the best-fit results of angle-dependent reflectivity spectra. Fitting curves of the LPB and UPB, together with the cavity mode  $E_c$  and energy of exciton resonance  $E_x$  are shown as a white dashed curves.

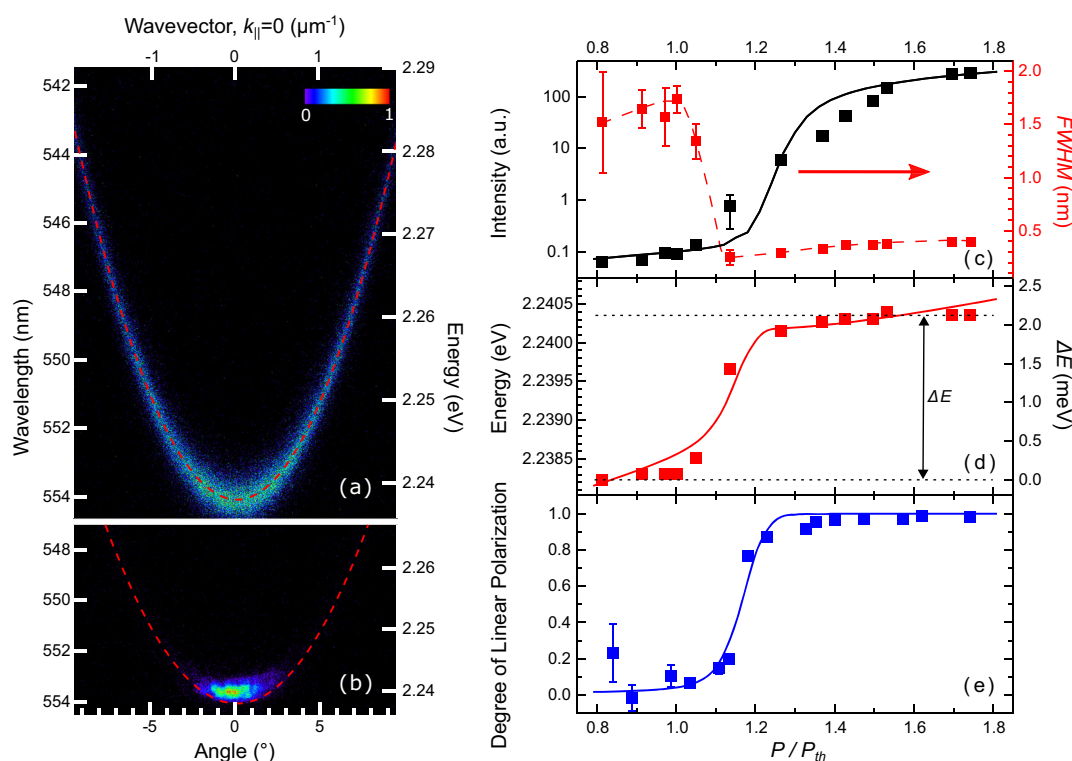


**Fig. 2 Non-equilibrium polariton condensation.** Normalized  $E, k$  polariton-population (photoluminescence) images recorded using Fourier-space imaging, below, at  $0.8P_{th}$  **(a)** and above condensation threshold, at  $1.4P_{th}$ , **(b)**. Dashed red curves show lower polariton branch dispersion in the linear regime. **c** Photoluminescence intensity at  $k_{||} \sim 0$ , integrated into the range over  $\pm 0.2 \mu\text{m}^{-1}$  (black squares) and full-width at half-maximum (FWHM, red squares) and **d** energy of the ground polariton state versus pump power. The superlinear increase and 10-fold linewidth narrowing together with high-energy shift of the polariton ground state observed above the threshold are commonly-recognised features of non-equilibrium polariton condensation. **e** Degree of linear polarization (blue squares) as a function of pump power, indicating that the condensate inherits the polarization of the pump beam. Solid curves in **c-e** represent numerical simulations of time-integrated photoluminescence, the ground state energy, and degree of linear polarization as functions of pump power, respectively. The red dashed curve in **c** is a guide for the eye. Error bars in **c, d** determined as standard deviations of the best-fit results of integrated photoluminescence intensity at different pump powers. Error bars in **d** are within the marker size. Error bars in **e** correspond to standard deviations of DLP obtained from photoluminescence intensities measured for orthogonal polarizations.

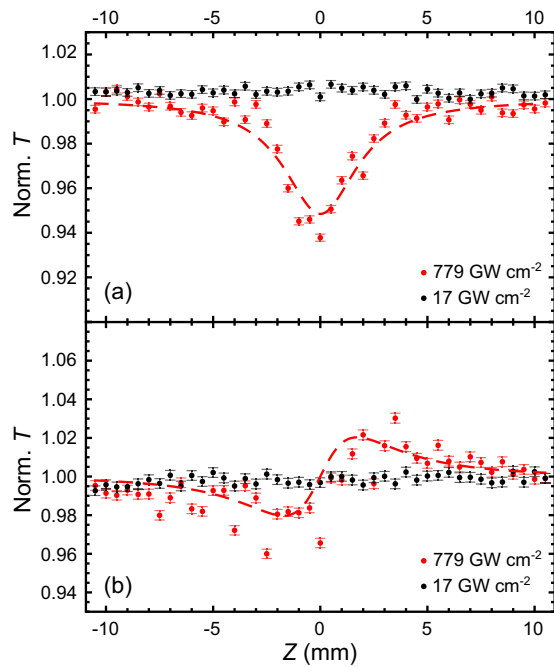


**Fig. 3 Nonlinear optical susceptibility of the neat film.** **a** Open aperture and **b** closed-aperture Z-scan data measured at two different incident pump energies 9.5 nJ (black circles) and 438 nJ (red rhombs). The fitting curves (red dashed) in **a**, **b** correspond to  $\text{Im}[\chi^{(3)}] = 1.71 \times 10^{-20} \text{ m}^2 \text{ V}^{-2}$  and  $\text{Re}[\chi^{(3)}] = 2.17 \times 10^{-20} \text{ m}^2 \text{ V}^{-2}$ , respectively. Error bars correspond to the standard deviation of a single Z-scan measurement on a glass substrate.

779  $\text{GW cm}^{-2}$  at the foci of the beam, we observe an optical nonlinearity in the form of reverse saturable absorption.

The closed-aperture Z-scan measurements presented in Fig. 3b provides a measure of the real part of the nonlinear optical susceptibility. Here, we do not detect any change in the nonlinear refractive index when pumping at the lower incident pulse energy. However, at the higher incident intensity of 779  $\text{GW cm}^{-2}$ , we find that the material exhibits a weak self-focusing effect from which we determine a positive nonlinear refractive index ( $n_2$ ) of  $\sim 1.89 \times 10^{-14} \text{ cm}^2 \text{ W}^{-1}$  (calculation is shown in Supplementary Note 4). We note that even if such high electromagnetic fields could be generated within a microcavity, the positive value of  $n_2$  that we determine would induce a redshift. We conclude, therefore, that the optically induced change of the intracavity nonlinear refractive index is not responsible for the blueshift observed at the condensation threshold.

**Gain-induced frequency pulling.** We now consider whether the gain-induced frequency pulling could be responsible for the blueshift at the condensation threshold. This mechanism is expected to be particularly important in negatively detuned microcavities in which the polariton mode has a large photonic fraction. We characterize the spectral distribution of the optical gain by recording amplified spontaneous emission (ASE) from a control (non-cavity) film of BODIPY-G1 dye molecules dispersed in a polystyrene matrix (see Supplementary Note 1 and Methods). A typical ASE spectrum is plotted in Fig. 4a [red line], where it can be seen that the emission (corresponding to the peak of optical gain) is peaked around 2.272 eV (545.8 nm).

We explore the extent to which gain-induced frequency pulling affects the condensate's blueshift by tuning the frequency of the lower polariton branch across the optical gain spectrum. Such tunability in the lower polariton branch wavelength is possible

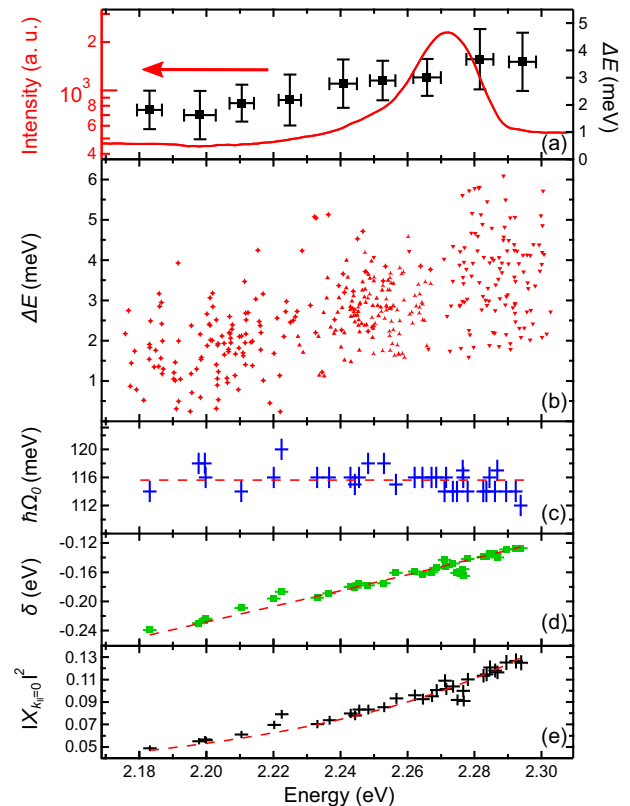


**Fig. 4 Blueshifts and the optical gain spectrum.** **a** The amplified spontaneous emission spectrum and the blueshift,  $\Delta E$ , extracted from the binning of scattering plot **(b)** that shows single-shot blueshift realizations across the whole sample area. **c** Vacuum Rabi splitting  $\hbar\Omega_0$  and **d** detuning  $\delta$  extracted from the multiple angle-dependent reflectivity measurements carried out across the sample area. The Rabi splitting remains constant across the whole-sample area with an average value of  $(116 \pm 1.5) \text{ meV}$  (red dashed curve). **e** The exciton fraction  $|X_{k_{||}=0}|^2$  of the polariton wave function at  $k_{||} = 0$ , calculated from  $\hbar\Omega_0$  and  $\delta$  shown above in **c** and **d**, respectively. Red dashed curves in **d** and **e** correspond to analytical fit functions for  $\delta$  and  $|X_{k_{||}=0}|^2$ , respectively. Error bars in **a** correspond to standard deviations of the blueshift (y-axis) and lower polariton state (x-axis) calculated for each binning range. Error bars in **c–e** correspond to standard deviations of the best-fit results of the angle-dependent reflectivity measurements.

through the variation in the thickness of the intracavity film across the sample. This effect allows us to explore polariton condensation over a broad range of exciton–photon detuning conditions. Figure 4b shows the measured energy shift for  $\sim 400$  single-shot measurements of polariton condensation at a wide range of different polariton ground state energies. For each measurement, the energy shift is defined by comparing the energy of the emission below and above the threshold. Here, we avoid averaging over the intensity fluctuations of the laser by utilizing a single-shot dispersion imaging technique. In Fig. 4a, we superimpose the measured blueshift using the Sturge binning rule with the amplified spontaneous emission spectrum (for details see Supplementary Note 2). It is apparent that at condensation threshold, the recorded energy shifts are always positive, and thus we conclude that the blueshift is not induced by gain frequency pulling. Indeed, if the gain-induced frequency pulling considerably contributes to polariton energy shifts, one would expect a negative sign of the shift observed for the left side of the ASE peak instead. However, we systematically observe polariton blueshifts regardless of the side of the gain peak.

**Polariton interactions.** We now investigate the possible contribution of polariton–exciton and pair-polariton scattering in determining the observed blueshift at the condensation threshold. In semiconductor microcavities containing Wannier–Mott excitons, the experimentally observed energy shifts ( $\Delta E$ ) are attributed to a combination of pair-polariton ( $g_{p-p} N_p$ ) and polariton–exciton ( $g_{p-x} N_x$ ) interaction terms. This is summarized by the following equation<sup>12,19</sup>:

$$\Delta E = g_{p-p} \cdot N_p + g_{p-x} \cdot N_x, \quad (1)$$

where the pair-polariton scattering interaction constant can be related to the exciton–exciton scattering constant ( $g_{x-x}$ ) using  $g_{p-p} = g_{p-x} \cdot |X|^2 = g_{x-x} \cdot |X|^4$ , where  $X$  is the amplitude of the exciton fraction that is mixed into a polariton state, and  $N_p$  and  $N_x$  are the polariton and exciton reservoir densities, respectively. Since the occupancy of polaritons at the condensation threshold does not depend on the exciton fraction, the measured dependence of the energy shift versus the square of the amplitude of the exciton fraction ( $|X|^2$ ) should reveal whether pair-polariton or polariton–exciton interactions dominate the blueshift.

To determine the dependence of the measured blueshift shown in Fig. 4b versus the exciton fraction, we need first to describe the dependence of the experimentally measured emission frequency of the polariton state on its exciton fraction. The latter depends on the exciton–photon detuning ( $\delta$ ) and vacuum Rabi splitting through  $|X_{k_{\parallel}=0}|^2 = \frac{1}{2} \left( 1 + \frac{\delta}{\sqrt{\delta^2 + (\hbar\Omega_0)^2}} \right)$ . To avoid any excitation density-dependent energy shifts of the lower polariton branch, we perform white light, angle-resolved reflectivity measurements across the available detuning range. We fit the linear polariton dispersions by varying the vacuum Rabi splitting and the exciton–photon detuning, while keeping the exciton energy and the effective refractive index of the intracavity layer constant (see Supplementary Note 2). Figure 4c, d plot the fitted values of vacuum Rabi splitting and exciton–photon detuning vs the energy of the polariton state. This analysis indicates that the vacuum Rabi splitting is virtually invariant across the whole sample area and has an average value of  $(116 \pm 1.5)$  meV, with the exciton–photon detuning spanning the range 120 meV,  $\delta \in [-240, -120]$  meV. From this, we plot the dependence of  $|X_{k_{\parallel}=0}|^2$  on the energy of the polariton state, as shown in Fig. 4e.

Using this approach, we can also determine the dependence of the measured energy shift,  $\Delta E$ , on  $|X_{k_{\parallel}=0}|^2$ , shown in Fig. 5. This indicates that the energy shift of the polaritons on condensation has a sub-linear dependence on  $|X_{k_{\parallel}=0}|^2$ ; a result that firmly precludes pair-polariton scattering as the underlying mechanism for the observed blueshift and suggests that polariton–exciton scattering is also unlikely; here the former process would result in a quadratic dependence on  $|X_{k_{\parallel}=0}|^2$  and the latter on a linear dependence (see Eq. (1)).

In the absence of pair-polariton interactions and for a constant exciton fraction/detuning (as expressed by Eq. (1)), we expect that polariton–exciton interactions should lead to a linear energy shift with increasing excitation and thus exciton density. At the condensation threshold, stimulated relaxation from the exciton reservoir to the polariton ground state would lead to clamping of the exciton density and, therefore, of the energy shift. However, to date, all non-crystalline semiconductor microcavities undergo a nearly step-like increase of polariton blueshift at condensation threshold<sup>3–9</sup>, as shown in Fig. 2d, subject to the accuracy of the measured excitation density. Thus, the step-like dependence precludes polariton–exciton interactions as the driving mechanism for the observed blueshifts; a conclusion that is also corroborated by the sub-linear dependence of the energy shift

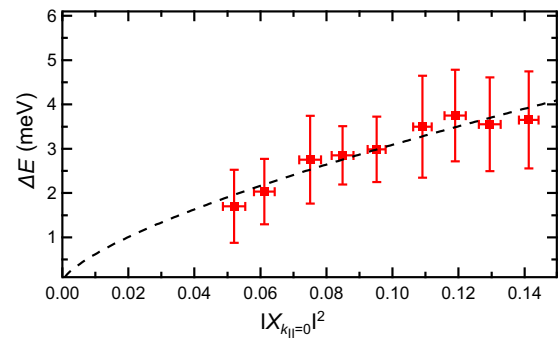


**Fig. 5 The blueshift  $\Delta E$  versus exciton fraction.** The dependence of the blueshift on the exciton fraction is calculated by binning the scattering plot of single-shot blueshift realizations across the whole accessible detuning range and taking into account the dependence of exciton fraction on the ground polariton state energy. The dashed black line is the best-fit result by power-law  $\Delta E \sim (|X_{k_{\parallel}=0}|^2)^\beta$  with variable parameter  $\beta = 0.7$ . Error bars correspond to standard deviations of the blueshift ( $y$ -axis) and exciton fraction ( $x$ -axis) calculated for each binning range.

on  $|X_{k_{\parallel}=0}|^2$ . Such a conclusion is also consistent with the high degree of localization of Frenkel excitons on a single molecule, as such exciton localization is expected to dramatically weaken Coulomb exchange interactions and suppress interparticle scattering.

**Saturation of molecular optical transitions.** In the following, we propose and experimentally verify that the observed blueshifts are due to quenching of the Rabi splitting and a nonlinear change of the cavity refractive index  $n_{\text{eff}}$ . Both mechanisms are a consequence of the same nonlinear process, namely saturation of molecular optical transitions. Owing to the Pauli-blocking principle, excited (i.e., occupied) states cannot be filled twice, thus effectively reducing the oscillator strength of Frenkel excitons. Therefore, occupied states do not contribute to optical absorption at the exciton resonance that in turn reduces the Rabi splitting<sup>4,20</sup> through the relation

$$\hbar\Omega = \hbar\Omega_0 \sqrt{1 - \frac{2(n_x + n_p)}{n_0}} \quad (2)$$

(for a microscopic theory of Rabi quenching see Supplementary Note 5). Here, Eq. (2) describes the quenching of the vacuum Rabi splitting,  $\hbar\Omega_0$ , as a function of the total number of excitations, namely the sum of excitons and polaritons  $n_x + n_p$ , where  $n_0$  is the total number of molecules contributing to strong coupling. Since the optical pump results in a saturation of the molecular optical transitions that contribute to strong coupling, we expect a partial quenching of the Rabi splitting; an effect that results in a measurable blueshift of the lower polariton mode with increasing excitation density. We note here that only a small fraction of molecules in the intracavity layer are strongly coupled to the cavity mode ( $f_c = \frac{n_0}{n_{\text{tot}}}$  is the fraction of coupled molecules), as was suggested by Agranovich et al.<sup>21</sup>. Therefore, a renormalization of the light-matter interaction constant originates exclusively from strongly coupled molecules, while the remaining weakly coupled molecules do not contribute to the blueshift through the Rabi quenching mechanism. However, non-resonant pumping leads to a uniform excitation of molecules across the intracavity volume and equally populates both strongly and weakly coupled molecules. Thus, the large amount of weakly coupled molecules dispersed in the cavity can contribute to the blueshift via the renormalization of the cavity mode energy that

occurs from the decrease of the intracavity effective refractive index,  $n_{\text{eff}}$ : a consequence of the quenching of the oscillator strength for the molecules' optical transition. Analogously, the effect of the carrier density-dependent nonlinear refractive index change on the polariton dispersion was recently shown in inorganic ZnO microcavities<sup>22</sup>. In weakly coupled microcavities, mode energy shifts induced by refractive index changes of the intracavity material have been used as a probe for the measurement of optical nonlinearities<sup>23</sup>.

The change in refraction under quenching of the oscillator strength is inherent to the causality principle, the Kramers–Kronig relation, that couples the real and imaginary parts of the complex dielectric function<sup>24</sup>. The relation predicts a decrease of the refractive index above the induced absorption resonance and an increase below the resonance, resulting in an anomalous dispersion that usually appears within the width of an optical transition. We address the problem of refractive index change by general Kramers–Kronig analysis:

$$n(\omega) = \frac{1}{\pi} \text{PV} \int_{-\infty}^{+\infty} \frac{k(\omega')}{\omega - \omega'} d\omega', \quad (3)$$

where PV stands for integration over the Cauchy principal value, and  $k(\omega)$  is an extinction coefficient, being an imaginary part of the refractive index.

In order to calculate the real part of the complex refractive index using Eq. (3), one needs to know the  $k(\omega')$ , which is related to the absorption spectrum. We use the absorption spectrum of the bare film to extract  $k(\omega)$ ; for details, see Supplementary Note 6. As the absorption spectrum can be perfectly decomposed by a couple of Gaussian distributions centered at 2.446 and 2.548 eV for the excitonic energy and its vibronic replica, respectively, it is quite convenient to calculate Eq. (3) through the known Hilbert transformation of Gaussians in the form of the weighted sum over the Dawson functions:

$$n(\omega) = -\frac{2}{\sqrt{\pi}} \sum_i A_i \cdot F \left[ \frac{(\omega - \omega_{o,i})}{\sigma_i \sqrt{2}} \right], \quad (4)$$

where the imaginary part is taken in the form of the sum over the Gaussian distributions  $k(\omega) = \sum_i A_i e^{-\frac{(\omega - \omega_{o,i})^2}{2\sigma_i^2}}$ , accordingly, and  $F \left[ \frac{(\omega - \omega_{o,i})}{\sigma_i \sqrt{2}} \right]$  is the Dawson function (integral) with an argument  $\frac{(\omega - \omega_{o,i})}{\sigma_i \sqrt{2}}$ .

Equation (4) describes the anomalous dispersion that naturally appears on the average effective cavity refractive index  $n_{\text{eff}} = 1.81$  as the consequence of the molecular optical transitions, see Supplementary Note 2. Therefore, with decreasing the imaginary part, one can observe a reduction in the real part of the refractive index over the lower energy sideband. Figure 6a shows the imaginary and real parts of the complex refractive index as a function of energy. Note that  $\Delta n$  is positive on the high-energy side of the exciton resonance and negative on the low-energy side.

The change in refractive index is evident over a range of energies on either side of the resonance that induces a correspondent energy shift of the cavity mode  $E_c$  by a value of  $\Delta E_c$ . For small changes of  $\Delta n \ll n_{\text{eff}}$ , one can approximate the energy shift with

$$\Delta E_c \cong -E_c \frac{\Delta n}{n_{\text{eff}}}, \quad (5)$$

where  $n_{\text{eff}} = 1.81$  is the effective cavity refractive index.

Equation (5) describes the blueshift of the lower polariton dispersion due to the change that occurs in the cavity refractive index from the saturation of weakly coupled molecular optical transitions. The net effect of both the quenching of the vacuum

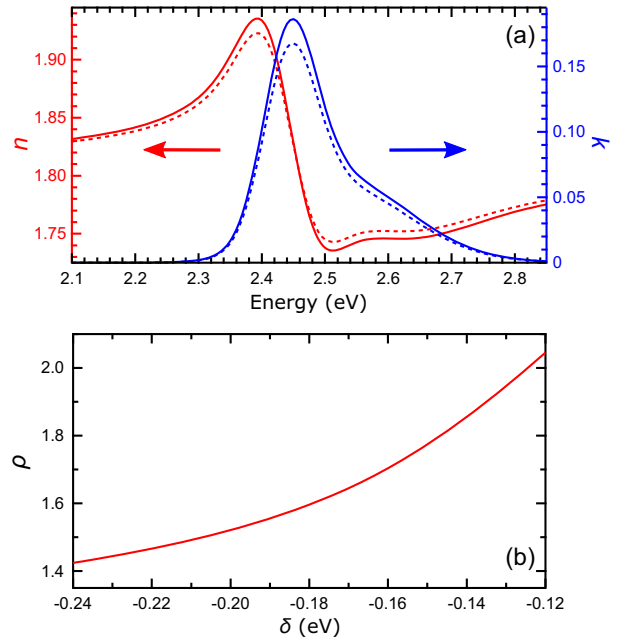


**Fig. 6 Kramers-Kronig analysis.** **a** Real (red) and imaginary (blue) parts of the complex refractive index plotted for the case of unperturbed (solid) and saturated (dashed) molecular transitions, respectively, where we saturate the transition by 10%. **b** The ratio  $\rho = \frac{\Delta E_{\text{LPB}}^c}{\Delta E_{\text{LPB}}^\Omega}$  shows the relative contributions of the cavity mode energy renormalization (numerator) and the Rabi-quenching term (denominator) to the overall polariton blueshift as a function of exciton-photon detuning.

Rabi splitting and cavity mode renormalization on the blueshift  $\Delta E_{\text{LPB}}$  is given by

$$\Delta E_{\text{LPB}} = 1/2 \cdot \left\{ E_x + E_c \left( 1 - \frac{\Delta n}{n_{\text{eff}}} \right) - \sqrt{\left( E_c \left( 1 - \frac{\Delta n}{n_{\text{eff}}} \right) - E_x \right)^2 + (\hbar\Omega)^2} \right\} - E_{\text{LPB}}^0 \quad (6)$$

where  $E_x, E_c$  are the energies of the bare exciton and cavity modes respectively, and  $E_{\text{LPB}}^0$  is the unperturbed energy of the ground polariton state in the limit of small excitation numbers (linear regime),  $\hbar\Omega$  and  $\Delta n$  are the density-dependent Rabi splitting and the change of cavity refractive index, respectively.

In the case of a small saturation parameter  $\xi$ , namely  $\xi = \frac{(n_x + n_p)}{n_0} \cong \frac{n_x}{n_0} \ll 1$ , we can significantly simplify the above equation for the polariton blueshift. First, we describe the change in refractive index  $\Delta n$  by means of parameter  $\xi$  as follows:

$$\Delta n = -\frac{\ln 10}{2\pi\sqrt{\pi}} \cdot \xi \cdot \alpha \cdot F[d] \cong -\frac{1}{5} \xi \cdot \alpha \cdot F[d]. \quad (7)$$

We replace the weighted sum over the Dawson functions from Eq. (4) to a single Dawson function with argument  $d = \frac{[\delta] \cdot 2\sqrt{\ln 2}}{\text{FWHM}}$ , where  $\delta = E_c - E_x$  is the detuning and the full-width at half-maximum (FWHM) of the main absorption peak which is attributed to the  $S_{0,0} \rightarrow S_{1,0}$  singlet optical transition. The scaling parameter  $\alpha$  in Eq. (7) corresponds to the oscillator strength of the optical transition as it is proportional to the absorption maximum ( $\text{Abs}_{\text{max}}$ ),  $\alpha = \frac{\text{Abs}_{\text{max}} \cdot \lambda_{\text{max}}}{L}$ , where  $L$  is the cavity thickness. Thus, we can now reformulate Eq. (6) for the total polariton blueshift in a more convenient way within the approximation of a small saturation parameter  $\xi$ :

$$\Delta E_{\text{LPB}} = \Delta E_{\text{LPB}}^\Omega + \Delta E_{\text{LPB}}^c = \frac{\xi s \cdot \hbar\Omega_0}{2\sqrt{1+s^2}} + \frac{\xi E_x - |\delta|}{2 \cdot 5 n_{\text{eff}}} F[d] \cdot \alpha \cdot \left( 1 + \frac{1}{\sqrt{1+s^2}} \right), \quad (8)$$

where  $s = \frac{\hbar\Omega_0}{|\delta|}$  is a dimensionless parameter of strong coupling; we exploit the reasonable assumption of  $f_c \ll 1$ .

Both terms in Eq. (8) reflect the influence of the same physical process of saturation of the optical transition on the polariton energy, but rely on different subsets of molecules. The first term corresponds to the quenching of the vacuum Rabi splitting in strongly coupled molecules. The second term corresponds to the renormalization of the cavity mode energy due to the change of the intracavity effective refractive index from the excitation of weakly coupled molecules. Surprisingly, we find that the renormalization of the cavity mode energy dominates over the quenching of the Rabi splitting in the total polariton blueshift as

$\rho = \frac{\Delta E_{\text{LPB}}^c}{\Delta E_{\text{LPB}}^o} = \frac{(E_x - \delta) \cdot F[d] \cdot \alpha \cdot (\sqrt{1+s^2} + 1)}{5n_{\text{eff}} \cdot s \cdot \hbar\Omega_0} > 1$  for the whole range of exciton–photon detuning accessible in this study. Clearly, the ratio is invariant over the saturation parameter  $\xi$ , and it depends on  $\hbar\Omega_0$ ,  $\delta$ , the absorption of the optical transition,  $\alpha$ , its linewidth FWHM and cavity thickness  $L$ . Figure 6b shows the  $\rho$  ratio versus the detuning. To the best of our knowledge, the significance of the renormalization of the cavity mode energy to the total energy shift of organic polariton condensates has not been considered to date. Although Eq. (8) ultimately describes the magnitude of blueshifts in strongly coupled organic microcavities, neither of the involved mechanisms nor their superposition can explain the ubiquitous step-like increase of the blueshift at condensation threshold,  $P_{\text{th}}$ , but instead predicts a continuous increase of the blueshift with an increasing number of excitations in the system, characterized by parameter  $\xi$ .

**Intermolecular energy transfer.** To explain the pump power dependence of polariton blueshifts, we construct a model that distinguishes between molecules that have a non-zero projection of their optical dipole moment aligned parallel ( $N_0^{\parallel}$ ) and perpendicular ( $N_0^{\perp}$ ) to the linear polarization of the excitation laser. We assume that upon non-resonant optical excitation, only parallel-aligned molecules are initially occupied. These molecules constitute an exciton reservoir ( $N_x^{\parallel}$ ) whose population is then depleted through: (i) energetic relaxation to the ground polariton state having the same optical alignment ( $N_p^{\parallel}$ ), (ii) intermolecular energy transfer to perpendicular-aligned molecules as well as to other uncoupled molecules having some out-of-plane projection of the dipole moment  $N_0^{\times}$  and (iii) decay via other nonradiative channels ( $\gamma_{\text{NR}}$ ). We propose that intermolecular energy transfer from exciton reservoir  $N_x^{\parallel}$  populates exciton reservoirs  $N_x^{\perp}$  and  $N_x^{\times}$ , whose populations are in turn depleted through the same energy relaxation channels with the  $N_x^{\perp}$  reservoir creating polaritons having an optical alignment that is perpendicular to the excitation laser ( $N_p^{\perp}$ ). Figure 7 shows a schematic of the involved molecular transitions and relaxation paths of excited states considered within our model.

In densely packed organic films, intermolecular energy transfer is an efficient process that results in the ultrafast depolarization of fluorescence<sup>25,26</sup>. When such films are embedded in a strongly coupled microcavity, intermolecular energy transfer below condensation thresholds is evidenced by a near-zero degree of linear polarization, as shown in Fig. 2e. With increasing excitation density and upon condensation threshold, energy relaxation to the ground polariton state becomes stimulated, resulting in sub-picosecond relaxation times, i.e., stimulated relaxation becomes faster than intermolecular energy transfer. Thereby, polariton condensation occurs with optical alignment parallel to the excitation laser<sup>3–5,8</sup>. The interplay between stimulated relaxation to the ground polariton state and intermolecular energy transfer can qualitatively describe the step-like increase of the degree of linear

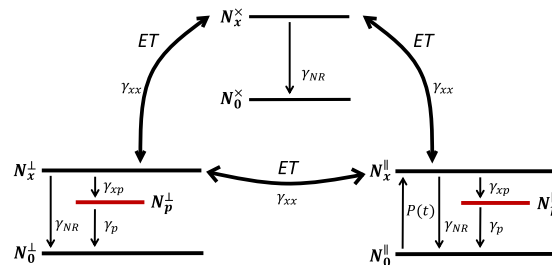


**Fig. 7** Schematic of the molecular transitions and relaxation paths of excited states considered within the model.

polarization at the condensation threshold, experimentally observed here in Fig. 2e. The quenching of intermolecular energy transfer upon condensation threshold, effectively increases the occupation of  $N_0^{\parallel}$ -molecules, which in turn quenches the corresponding Rabi splitting,  $\hbar\Omega^{\parallel} = \hbar\Omega_0^{\parallel} \sqrt{1 - \frac{2(N_x^{\parallel} + N_p^{\parallel})}{N_0^{\parallel}}}$ , and blueshifts the ground polariton state accordingly, by  $\Delta E_{\text{LPB}}^{\Omega} = 1/2 \cdot (E_x + E_c - \sqrt{(E_c - E_x)^2 + (\hbar\Omega^{\parallel})^2}) - E_{\text{LPB}}^0$ , where  $E_x$  and  $E_c$  are the energies of the bare exciton and cavity modes respectively, and  $E_{\text{LPB}}^0$  is the energy of ground polariton state in the limit of small excitation numbers (linear regime). Analogously, the blueshift accompanied with renormalization of the cavity mode energy can be described by the density-dependent function  $\Delta E_{\text{LPB}}^c = 1/2 \cdot \left\{ E_x + E_c \left(1 - \frac{\Delta n}{n_{\text{eff}}}\right) - \sqrt{(E_c \left(1 - \frac{\Delta n}{n_{\text{eff}}}\right) - E_x)^2 + (\hbar\Omega_0^{\parallel})^2} \right\} - E_{\text{LPB}}^0$ , where  $\Delta n$  is defined by Eq. (7). In the case of small saturation, namely  $\frac{(N_x^{\parallel} + N_p^{\parallel})}{N_0^{\parallel}} \ll 1$ , the net polariton blueshift  $\Delta E_{\text{LPB}}$  is just a linear superposition of both contributions:  $\Delta E_{\text{LPB}}^{\Omega} + \Delta E_{\text{LPB}}^c$  that is described by Eq. (8). The competition between stimulated relaxation to the ground polariton state and intermolecular energy transfer qualitatively predicts the saturation of molecular optical transitions that are optically aligned with the excitation laser, and the concomitant step-like energy shift at condensation threshold, as shown in Fig. 2d.

To quantitatively describe the experimental dependence of the polariton emission intensity, energy shift, and degree of linear polarization with increasing excitation density, shown in Fig. 2c–e, we formulate the above model in terms of coupled rate equation (for more information see Supplementary Note 7):

$$\begin{aligned} \frac{dN_0^{\parallel, \perp, \times}}{dt} &= -P^{\parallel, \perp}(t)N_0^{\parallel, \perp}(t) + N_p^{\parallel, \perp}(t)\gamma_p + N_x^{\parallel, \perp, \times}(t)\gamma_{\text{NR}} \\ &\quad + N_x^{\parallel, \perp, \times}(t)2\gamma_{\text{xx}} - N_x^{\times, \parallel, \perp}(t)\gamma_{\text{xx}} - N_x^{\perp, \times, \parallel}(t)\gamma_{\text{xx}} \\ \frac{dN_x^{\parallel, \perp, \times}}{dt} &= P^{\parallel, \perp}(t)N_0^{\parallel, \perp}(t) - N_x^{\parallel, \perp}(t)\{N_p^{\parallel, \perp}(t) + 1\}\gamma_{\text{xp}} \\ &\quad - N_x^{\parallel, \perp, \times}(t)2\gamma_{\text{xx}} + N_x^{\times, \parallel, \perp}(t)\gamma_{\text{xx}} + N_x^{\perp, \times, \parallel} \\ &\quad \times (t)\gamma_{\text{xx}} - N_x^{\parallel, \perp, \times}(t)\gamma_{\text{NR}} \\ \frac{dN_p^{\parallel, \perp}}{dt} &= N_x^{\parallel, \perp}(t)\{N_p^{\parallel, \perp}(t) + 1\}\gamma_{\text{xp}} - N_p^{\parallel, \perp}(t)\gamma_p \end{aligned} \quad (9)$$

where  $P^{\parallel, \perp}(t)$  is the term corresponding pulsed optical excitation, in the case of linearly polarized pump  $P^{\perp}(t) = 0$ ,  $\gamma_{\text{NR}} = 2.5 \times 10^8 \text{ s}^{-1}$  is the nonradiative decay rate of the exciton reservoirs,  $\gamma_p = 10^{13} \text{ s}^{-1}$  is the polariton decay rate,  $\gamma_{\text{xx}} = 3.33 \times 10^{10} \text{ s}^{-1}$  are decay rates of intermolecular energy transfer between  $N_x^{\parallel}$ ,  $N_x^{\perp}$  and  $N_x^{\times}$ ,  $\gamma_{\text{xp}} = 1.75 \times 10^5 \text{ s}^{-1}$  is the relaxation

rate from exciton reservoirs ( $N_x^{\parallel}$ ,  $N_x^{\perp}$ ) towards the ground polariton states ( $N_p^{\parallel}$ ,  $N_p^{\perp}$ ), respectively. In the energy relaxation from the exciton reservoir to the ground polariton state, we have included a stimulation term  $N_x^{\parallel,\perp}(t)\{N_p^{\parallel,\perp}(t) + 1\}\gamma_{xp}$ . The solid lines in Fig. 2c–e show the result of the numerical simulations, where we find good quantitative agreement with the experimental observations by using two variable parameters, namely the exciton to polariton relaxation rate ( $\gamma_{xp}$ ) and the fraction of strongly coupled molecules ( $f_c$ ). We note that by switching off intermolecular energy transfer ( $\gamma_{xx} = 0$ ), we obtain a linear dependence of the energy shift with increasing excitation density that saturates above condensation threshold, see Supplementary Note 7.

## Discussion

We further extend our analysis to another strongly coupled organic microcavity with less than half the BODIPY-G1 concentration, ~4%. With decreasing dye concentration, we observe a reduction of the vacuum Rabi splitting from 116 meV, for the 10% sample, to 72 meV for the 4% sample, see Supplementary Note 8. For the 4% sample, we observe ~27% lower absorbed pump power at the condensation threshold of the same exciton fraction presumably due to the inverse dependence of the film's quantum yield on dye concentration. We thus obtain that at the condensation threshold, the saturation of the molecular optical transitions is twice stronger for the 4% sample, and therefore we expect a stronger blueshift. Figure 8a shows the experimentally measured blueshift versus threshold pump power both for the 10% (red) and the 4% (blue) samples at detuning conditions that correspond to equal exciton fractions  $|X_{k_{\parallel}=0}|^2 \cong 0.05$ , where indeed we observe a stronger blueshift for the 4% sample. The solid lines in Fig. 8a correspond to numerical simulations containing a density-dependent energy shift due to Rabi quenching and the renormalization of the cavity mode energy. Since the 4% sample exhibits smaller exciton–photon detuning (by means of its modulus  $|\delta|$ ), we observe a stronger impact of the cavity mode energy renormalization term on the overall polariton shift (see Supplementary Note 8). The higher blueshift in the 4% sample is consistent across the whole accessible range of exciton fractions in the two samples. Figure 8b demonstrates blueshifts as a function of exciton fraction  $|X_{k_{\parallel}=0}|^2$  plotted for the 4% (blue) and 10% (red) samples, respectively. We fit the data using Eq. (8), wherein the saturation parameter  $\xi$  is the only variable and considering nearly constant condensation threshold across the whole range of available detuning values, in agreement with our experimental observations (see Supplementary Note 9). According to the best-fit results, at the condensation threshold, we saturate the optical transitions for  $\xi_{10\%} = 0.03$  and  $\xi_{4\%} = 0.06$  for 10% and 4% samples respectively which is in excellent agreement with experimental assessment above  $\xi_{4\%}/\xi_{10\%} \cong 2$ . In the particular case of  $|X_{k_{\parallel}=0}|^2 \cong 0.05$ , we obtain similar contributions from the Rabi quenching for both samples (see Supplementary Note 10), while the renormalization of the cavity mode energy in both cases produces a stronger polariton blueshift. The larger polariton blueshifts for the “diluted” system elucidates the importance of uncoupled molecules in the observed energy shifts in organic microcavities. Under non-resonant optical pumping, uncoupled molecules contribute to energy shifts via the change of the intracavity refractive index through the saturation of their optical transition leading to a non-monotonous dependence on the exciton fraction, see Supplementary Note 10.

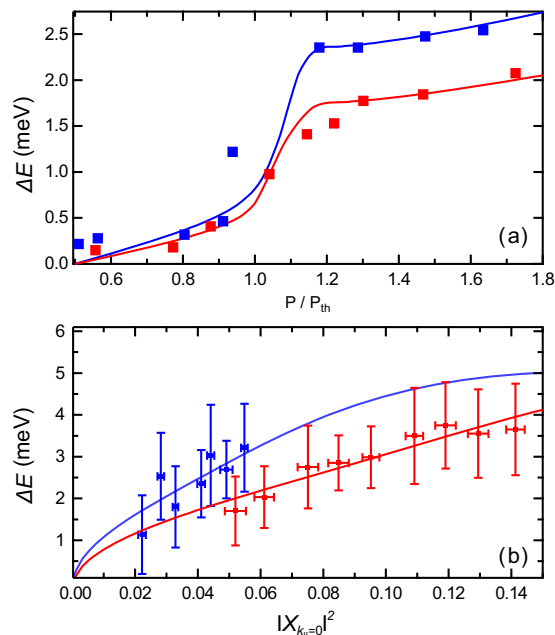


**Fig. 8 a** The data for polariton blueshifts acquired for 4% (blue) and 10% (red) samples plotted as a function of threshold pump power. Blue and red solid curves represent numerical simulations of time-integrated blueshifts, respectively. The error bars are within the marker size and correspond to standard deviations of the best-fit results of the peak energies. **b** The blueshift  $\Delta E$  versus exciton fraction for 4% (blue) and 10% (red) samples, solid curves show the best-fit results according to Eq. (8). Error bars in **b** correspond to standard deviations of the blueshift (y-axis) and exciton fraction (x-axis) determined for each binning range.

Unlike inorganic semiconductor microcavities that bear Wannier–Mott excitons, interparticle Coulomb exchange interactions are virtually absent in organic microcavities due to the localized nature of Frenkel excitons in molecular semiconductors. In the absence of Coulomb interactions, we have explained the origin of blueshifts in organic semiconductor microcavities and the step-like energy shift at the condensation threshold via the interplay of vacuum Rabi splitting, renormalization of cavity mode energy, and intermolecular energy transfer. The ultrafast energy migration mechanism is omnipresent in densely packed organic films and underlies the rapid depolarization of the emission upon optical excitations. We have shown that the step-like blueshift occurs at the condensation threshold when stimulated relaxation of optically aligned excitons to the ground polariton state exceeds the rate of intermolecular energy transfer. The interplay of intermolecular energy transfer and stimulated exciton relaxation predicts a step-like increase of the degree of linear polarization related to the step-like blueshift at the condensation threshold that is also observed experimentally. We constructed a simple model of the transient dynamics of optically aligned excitons and polaritons that reproduces qualitatively and quantitatively the ubiquitous step-like blueshift at the condensation threshold in non-crystalline organic microcavities. We also derived an analytic expression that allows for the evaluation of the relative contribution of the saturation of molecular optical transitions to the experimentally observed polariton blueshifts through Rabi quenching and cavity mode energy renormalization. Since polariton condensation is not a prerequisite for cavity mode energy renormalization, the experimental observation of blueshifts at the onset of nonlinear emission in

organic microcavities does not provide a sufficient condition in distinguishing between polariton condensation and lasing in the weak-coupling regime.

## Methods

**BODIPY-G1 neat film preparation.** Polystyrene (PS) with an average molecular weight of ( $M_w$ )  $\approx 192,000$  was dissolved in toluene at  $35 \text{ mg mL}^{-1}$  following heating at  $70^\circ\text{C}$  and stirring for 30 min. BODIPY-G1 (1,3,5,7-tetramethyl-8-phenyl-4,4-difluoroboradiazaindacene) was then dispersed into the PS/toluene inert matrix solution at 10% concentration by mass. The PS/BODIPY-G1 blend was spin-cast onto quartz-coated glass substrates to create neat thin films for absorption, photoluminescence, ASE, and nonlinear Z-scan measurements. The rotation speed was tuned between 4300 and 7900 RPM with the substrates being held on the rotating plate by a vacuum chuck and spun for 50 s before they dried.

**Microcavity fabrication.** The studied microcavities utilized double DBR mirrors with the bottom DBR having 10 pairs of alternate layers of  $\text{SiO}_2/\text{Nb}_2\text{O}_5$  and the top DBR having 8 pairs. The dielectric materials were deposited with an ion-assisted electron beam ( $\text{Nb}_2\text{O}_5$ ) and reactive sublimation ( $\text{SiO}_2$ ). The deposition of dielectric materials initiated at a chamber pressure of  $8 \times 10^{-6}$  mbar with a deposition rate of  $2 \text{ \AA s}^{-1}$  for  $\text{Nb}_2\text{O}_5$  and  $10 \text{ \AA s}^{-1}$  for  $\text{SiO}_2$ . The bottom mirror was deposited on a quartz-coated glass substrate. A layer of PS/BODIPY-G1 was then spin-cast on top of the bottom DBR. The thickness of the organic active layer was controlled via the rotation speed of the spin coater to achieve  $\lambda/2$  microcavities. The rotation speed was tuned between 4300 and 7900 RPM with the substrates being held on the rotating plate by a vacuum chuck and spun for 50 s before they dried. A thickness gradient, occurring from the spin-casting process, permitted different photon-exciton detuning values. For the deposition of the top DBR, the ion gun was kept turned-off for the first few layers of  $\text{Nb}_2\text{O}_5/\text{SiO}_2$  to avoid any damage on the organic active layer.

**Linear spectroscopy.** Absorption (Abs) of the bare BODIPY-G1 thin film was measured using a Fluoromax 4 fluorometer (Horiba) equipped with an Xe-lamp. Photoluminescence (PL) of the film was measured using an Andor Shamrock CCD spectrometer following 473 nm laser diode optical excitation. For absorption and photoluminescence spectra, see Supplementary Fig. 1.

A fiber-coupled halogen–deuterium white light source (Ocean Optics DH-2000) was used for the angular reflectivity measurements. Two motorized optical rails connected to two concentric rotation mounts allowed the illumination of the sample at different angles and the collection of the reflected white light accordingly. An attached fiber bundle at the end of the collection optical rail was used to direct light into an Andor Shamrock charge-coupled device (CCD) spectrometer. The polariton modes were fitted with Lorentzian curves in order to extract the energy of the LPB and UPB at different angles.

**Single-pulse dispersion imaging.** We investigated polariton condensate emission using 2 ps single pulses optical excitation from a Ti:Sapphire laser (Coherent Libra-HE), which was frequency-doubled through a barium borate crystal providing a wavelength of 400 nm. The pump beam was focused onto a sample by Nikon Plan Fluor 4X microscope objective in  $12 \mu\text{m}$  pump spot size at FWHM. Photoluminescence was collected in transmission configuration using Mitutoyo Plan Apo 20X microscope objective with a numerical aperture of 0.42. To block the residual light from the excitation beam, a Semrock LP02-442RU long-pass filter was used in the collection path. Filtered photoluminescence from a microcavity was coupled into a 750 mm focal length spectrometer (Princeton Instruments SP2750) equipped with an electron-multiplying CCD camera (Princeton Instruments ProEM-HS 1024  $\times$  1024). In all, 1200 grooves  $\text{mm}^{-1}$  grating and  $20 \mu\text{m}$  entrance slit were used to achieve a spectral resolution of 30 pm.

**ASE measurements.** ASE measurements were performed using a 355 nm pulsed laser with 350 ps pulse width and 1 kHz repetition rate. A 25 mm cylindrical lens was used to focus the beam on the sample creating a stripe excitation profile ( $1470 \mu\text{m} \times 80 \mu\text{m}$ ). ASE emission from the neat 172 nm thin film was detected from the edge of the film, in a direction perpendicular to that of the propagation of the incident pump beam. An Andor Shamrock CCD spectrometer was used to record ASE spectra. The power threshold for ASE was defined at  $P_{\text{th}} = 6 \text{ mW}$ . For ASE spectra, see Supplementary Fig. 2.

**Z-scan measurements.** We studied two thin films of BODIPY-G1 in polystyrene host matrix and polystyrene film itself, both 600 nm thickness. Measurements were carried out using an optical parametric amplifier (Coherent OPerA SOLO) pumped by the high-energy Ti:sapphire regenerative amplifier system (Coherent Libra-HE) with the central wavelength emission at 545 nm coinciding with the photon energy of the particular polariton condensate realization. Pulse duration and repetition rate were 140 fs and 10 Hz, respectively. The beam was tightly focused by 100 mm focal length lens resulting in  $16 \mu\text{m}$  spot radius. Data acquisition was performed using Si photodetectors (Thorlabs-Det10/M) connected with an oscilloscope

(Keysight DSOX3054T). For a sketch of the Z-scan experimental setup, see Supplementary Fig. 3.

## Data availability

The data that support the findings of this study are available in University of Southampton Institutional Repository with the identifier <https://doi.org/10.5258/SOTON/D1159>.

Received: 31 July 2019; Accepted: 17 December 2019;

Published online: 22 January 2020

## References

- Lidzey, D. G. et al. Strong exciton–photon coupling in an organic semiconductor microcavity. *Nature* **395**, 53–55 (1998).
- Kéna-Cohen, S. & Forrest, S. R. Room-temperature polariton lasing in an organic single-crystal microcavity. *Nat. Photonics* **4**, 371–375 (2010).
- Plumhof, J. D., Stöferle, T., Mai, L., Scherf, U. & Mahr, R. F. Room-temperature Bose–Einstein condensation of cavity exciton–polaritons in a polymer. *Nat. Mater.* **13**, 247–252 (2014).
- Daskalakis, K. S., Maier, S. A., Murray, R. & Kéna-Cohen, S. Nonlinear interactions in an organic polariton condensate. *Nat. Mater.* **13**, 271–278 (2014).
- Dietrich, C. P. et al. An exciton-polariton laser based on biologically produced fluorescent protein. *Sci. Adv.* **2**, e1600666 (2016).
- Cookson, T. et al. A yellow polariton condensate in a dye filled microcavity. *Adv. Opt. Mater.* **5**, 1700203 (2017).
- Sannikov, D. et al. Room temperature broadband polariton lasing from a dye-filled microcavity. *Adv. Opt. Mater.* **7**, 1900163 (2019).
- Rajendran, S. K. et al. Low threshold polariton lasing from a solution-processed organic semiconductor in a planar microcavity. *Adv. Opt. Mater.* **7**, 1801791 (2019).
- Zasedatelev, A. V. et al. A room-temperature organic polariton transistor. *Nat. Photonics* **13**, 378–383 (2019).
- Lerario, G. et al. Room-temperature superfluidity in a polariton condensate. *Nat. Phys.* **13**, 837–841 (2017).
- Vladimirova, M. et al. Polariton-polariton interaction constants in microcavities. *Phys. Rev. B* **82**, 075301 (2010).
- Sun, Y. et al. Direct measurement of polariton–polariton interaction strength. *Nat. Phys.* **13**, 870–875 (2017).
- Houdré, R. et al. Measurement of cavity polariton dispersion curve. *Phys. Rev. Lett.* **73**, 2043 (1994).
- Skolnick, M. S., Fisher, T. A. & Whittaker, D. M. Strong coupling phenomena in quantum microcavity structures—Abstract. *Semicond. Sci. Technol.* **13**, 645–669 (1998).
- Ciuti, C., Savona, V., Piermarocchi, C., Quattropani, A. & Schwendimann, P. Role of the exchange of carriers in elastic exciton-exciton scattering in quantum wells. *Phys. Rev. B* **58**, 7926–7933 (1998).
- Agranovich, V. M. & Tshich, B. S. Collective properties of Frenkel excitons. *Sov. Phys. JETP* **26**, 104 (1968).
- Litinskaya, M. Exciton polariton kinematic interaction in crystalline organic microcavities. *Phys. Rev. B* **77**, 155325 (2008).
- Sheik-bahae, M., Said, A. A. & Van Stryland, E. W. High-sensitivity, single-beam  $n_2$  measurements. *Opt. Lett.* **14**, 955 (1989).
- Kavokin, A., Baumberg, J. J., Malpuech, G. & Laussy, F. P. *Microcavities* (Oxford University Press, 2007).
- Brichkin, A. S., Novikov, S. I., Larionov, A. V. & Kulakovskii, V. D. Effect of Coulomb interaction on exciton-polariton condensates in GaAs pillar microcavities. *Phys. Rev. B* **84**, 195301 (2011).
- Agranovich, V. M., Litinskaia, M. & Lidzey, D. G. Cavity polaritons in microcavities containing disordered organic semiconductors. *Phys. Rev. B* **67**, 085311 (2003).
- Michalsky, T., Wille, M., Grundmann, M. & Schmidt-Grund, R. Spatiotemporal evolution of coherent polariton modes in ZnO microwire cavities at room temperature. *Nano Lett.* **18**, 6820–6825 (2018).
- Gulde, S., Jochim, S., Moll, N. & Mahr, R. F. A pump-and-probe method for the characterization of nonlinear material parameters within Fabry-Pérot microcavities. *J. Appl. Phys.* **100**, 043112 (2006).
- Peyghambarian, N., Koch, S. & Mysyrowicz, A. *Introduction to Semiconductor Optics* (Prentice Hall, 1993).
- Chang, M. H., Frampton, M. J., Anderson, H. L. & Herz, L. M. Intermolecular interaction effects on the ultrafast depolarization of the optical emission from conjugated polymers. *Phys. Rev. Lett.* **98**, 02742 (2007).
- Musser, A. J. et al. Intermolecular states in organic dye dispersions: excimers vs. aggregates. *J. Mater. Chem. C* **5**, 8380–8389 (2017).

## Acknowledgements

We thank Professor Nikolay Gippius for helpful discussions. A.Z. and A.B. acknowledge financial support from the Russian Scientific Foundation (RSF) grant No. 18-72-00227. O.K. and I.S. acknowledge support from the Government of the Russian Federation (projects 14.Y26.31.0015 and 3.2614.2017/4.6) and ITMO Fellowship Program. We also acknowledge partial funding from the UK EPSRC via Programme Grant “Hybrid Polaritonics” EP/M025330/1.

## Author contributions

D.L. designed the organic microcavity structures and supervised sample fabrication within the project; K.G. fabricated the neat PS/BODIPY-G1 films and organic microcavities, performed linear measurements of absorbance and emission the neat films as well as angle-dependent reflectivity and emission spectra of microcavities, and conducted ASE measurements; L.G. and Z.S. synthesized BODIPY-G1 dye. T.Y. and D.S. made analysis of angle-dependent reflectivity and extracted parameters of strong light-matter interaction, designed polarization-resolved single-pulse dispersion imaging setup, conducted the pump power measurements, and analyzed the data; T.Y. conducted detuning dependent measurements and performed statistical analysis of blueshifts; A.B. contributed with automation the experiments, conducted Z-scan measurements, analyzed the data and together with A.Z. determined role of optical Kerr effect; O.K. and I.S. developed microscopic model of vacuum Rabi-quenching; A.Z. contributed with the results interpretation and data analysis, developed model for blueshifts and polarization properties of the condensate, carried out the numerical simulations; P.L. supervised the research; T.Y., A.Z., and P.L. wrote the paper with input from all authors. T.Y., D.S., and A.Z. contributed equally to this work.

## Competing Interests

The authors declare no competing interests.

## Additional information

**Supplementary information** is available for this paper at <https://doi.org/10.1038/s42005-019-0278-6>.

**Correspondence** and requests for materials should be addressed to A.Z.

**Reprints and permission information** is available at <http://www.nature.com/reprints>

**Publisher's note** Springer Nature remains neutral with regard to jurisdictional claims in published maps and institutional affiliations.



**Open Access** This article is licensed under a Creative Commons Attribution 4.0 International License, which permits use, sharing, adaptation, distribution and reproduction in any medium or format, as long as you give appropriate credit to the original author(s) and the source, provide a link to the Creative Commons license, and indicate if changes were made. The images or other third party material in this article are included in the article's Creative Commons license, unless indicated otherwise in a credit line to the material. If material is not included in the article's Creative Commons license and your intended use is not permitted by statutory regulation or exceeds the permitted use, you will need to obtain permission directly from the copyright holder. To view a copy of this license, visit <http://creativecommons.org/licenses/by/4.0/>.

© The Author(s) 2020